An Analysis Method for the Transverse Beam Coupling Impedance of Asymmetric Structures using the Coaxial Wire Method

Hugo Alistair Day[a,b,c,*], Elias Métral[c], Fritz Caspers[c], Benoit Salvant[c], Roger Jones[a,b]

[a]*School of Physics and Astronomy, The University of Manchester, Oxford Road, Manchester, M13 9PL, UK*
[b]*Cockcroft Institute of Science and Technology, Daresbury, WA4 4AD, UK*
[c]*CERN-European Organization for Nuclear Research, Geneva, Switzerland*

Abstract

The analysis of data from the measurement of device impedance using the coaxial wire technique require a degree of understanding of both what is actually being measured by the method, and of what is being defined as a real and imaginary impedance. Through my own work I discovered a lack of clear definitions of how the data measured directly related to the quantities that we refer to from the point of view of particle motion. The idea of this document is to attempt to clarify how the quantities are related, and also give a clear guide as to how to analyse the experimental data to be compatible with a beam dynamics point of view. This presently a work in progress

Keywords: beam coupling impedance, coaxial wire technique, impedance measurements, asymmetric

*Corresponding author
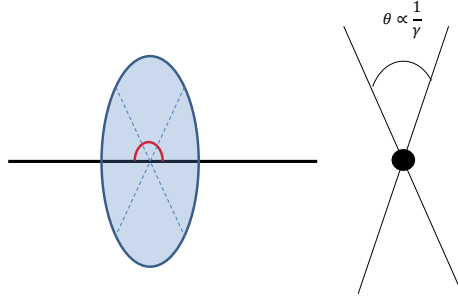Email address:* hday@hep.manchester.ac.uk (Hugo Alistair Day)

Figure 1: Comparison of the electromagnetic field profile of a moving charged particle and a short time pulse propagating along a coaxial wire.

Due to the sensitivity of the beam coupling impedance to the boundary conditions of the equipment used, it is necessary to utilise different measurement techniques to fully analyse the impedance of accelerator structures.

1. Low Q-factor Impedances

For structures that are expected to contain mostly low Q-resonances (i.e. resistive wall impedance) it is appropriate to use the coaxial wire method [1, 2], sometimes also called the stretched wire method. This method relies on the similarity of the electromagetic field profile due to an ultrarelativistic charged particle and that of a short electrical pulse sent along a coaxial wire.

A moving charged particle produces an electromagnetic field in a arc transverse to its direction of motion, where the angle of the arc opening is proportinal to the relativistic factor of the particle γ. For an ultrarelativistic particle ($\gamma \leftarrow \infty$), the field becomes entirely perpendicular to the direction of motion. If we place a conductive wire along the same path we would expect the charged particle to take (in most cases this is well represented by a straight wire), a short electrical pulse sent along this wire would propogate in the TEM (transverse electrical and magnetic field) mode, producing a field profile similar to that emitted by the ultrarelativistic charged particle (see. Fig. 1)

1.1. Classical Coaxial Wire Method

The classical coaxial wire method, first proposed in it's present form by V. Vaccarro in 1990 [2], is a transmission method that measures the complex transmission coefficient of a DUT (Device Under Test) made up of the equipment whose impedance is to be measured and a coaxial wire passing through it.

The experimental setup is as shown in Fig. 2. Firstly the external circuit (i.e. everything not the DUT) is matched to the characteristic impedance of the coaxial line inside the DUT. This is done by measuring the reflection coefficient Γ for the setup with only one port connected to the DUT and the other end
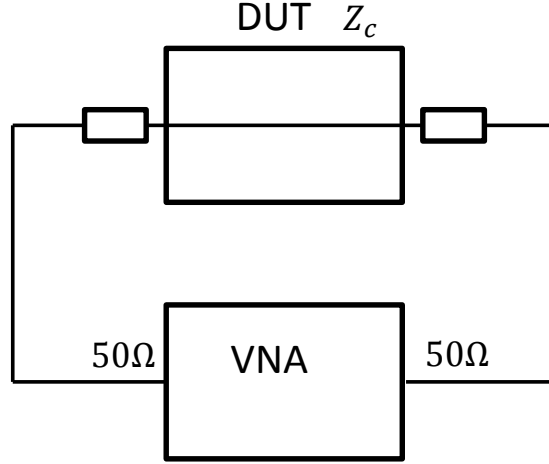
Figure 2: Experimental setup for a measurement of the beam coupling impedance using the classical coaxial wire method

terminated by an open connection. Knowing the characteristic impedance of the VNA and associated cables (typically $Z_0 = 50\Omega$), we can easily calculate the characteristic impedance, Z_c, from the relation,

$$\Gamma = \frac{Z_c - Z_0}{Z_c + Z_0}. \tag{1}$$

We then electrically match the characteristic impedance by adding resistors in series just before the DUT to resistively match the characteristic impedance of the VNA to that of the DUT. It is possible to use physical matching also using transition cones but these are costly, time consuming to construct and require new cones for each piece of equipment measured. And as can be seen in Fig. 3, matching with a resistor is highly effective at removing the presence of reflections in coaxial measurements.

The value that we wish to measure to evaluate the beam coupling impedance of a device are the scattering parameters of the resulting circuit, in particular S_{21}, the normalised transmission parameter through the DUT. S_{21} is calculated by taking the measured transmission parameter $S_{21,DUT}$ and dividing it by the transmission parameter through a reference line of the same physical length as the DUT,

$$S_{21} = \frac{S_{21,DUT}}{S_{21,REF}} \tag{2}$$

.

The effect of this is to correct the measured phase change in the DUT to be that only caused by the imaginary component of the beam coupling impedance.

There are subsequently a number of ways to evaluate the beam coupling impedance of the DUT depending on it's expected properties. For devices that are expected to have a either a small impedance, or those that are physically very short in length, it is possible to use the so called lumped impedance formula [3?];

Figure 3: An example of a reflection measurement made with and without a matching resistor. The faded line is the measurement with matching, the bold line that without. The reduction in the reflection can be seen due to the flatter line after the initial reflection.

$$Z = 2Z_c \frac{1 - S_{21}}{S_{21}} \tag{3}$$

.

For distributed impedances, it is suitable to use the so called log formula (called so due to attenuation causing a log function to appear in the evaluation) [3? , 4],

$$Z = -2Z_c ln\left(S_{21}\right) \tag{4}$$

.

For long components or measurements at very high frequencies there exists the improved log formula. This takes into account more completely the electrical length of the device, given by

$$Z = -2Z_c ln\left(S_{21}\right)\left(1 + j\frac{ln\left(S_{21}\right)}{2\Theta}\right) \tag{5}$$

where $\Theta = 2\pi\frac{L}{\lambda}$ is the normalised electrical length of the device, L the length of the device, λ the wavelength of the frequency of measurement. It is possible to see that the lumped impedance formula can be used when $\Theta \leq 1$, and the improved log formula becomes useful for $\Theta \geq 5$ [4].

1.2. Resonator Coaxial Wire Method

An alternative method for measuring the beam coupling impedance is by using the so called resonator method. The setup for this method is similar to that of the classical coaxial wire method, except that the matching resistor network between the VNA and DUT is replaced by a weak capacitive coupling ($S_{11} < 0.5dB$, remembering that $0dB$ means full reflection, i.e. no coupling) at both ends of the DUT. This then produces a structure which resonates at frequencies where the wavelength corresponds to the classical closed structure form,

4

$$\lambda = \frac{2L}{n} \tag{6}$$

where λ is the wavelength of the resonance, n the harmonic of the resonance and L the length of the device.

The resonant method enables accurate measurement of the transmission losses due to the real longitudinal impedance. Additional advantages are that no matching is required, and a large number of mechanical uncertainties (electrical connections, consistency of calibration) can be avoided. However it can be seen that the frequency resolution is limited due to the length of the DUT so the method is not recommended as the only measurement method for structures expected to contain high-Q, narrowband resonances. It can however be used to corroborate the results obtained using the classical method.

For each resonant peak, the loaded Q-factor and the frequency of the resonance are measured. For a weak coupling at both ends of the DUT, we can write the coupling coefficient k as

$$k = \frac{|S_{21}|}{1 - |S_{21}|}. \tag{7}$$

The difference between the unloaded Q-factor, Q_0, and the loaded Q-factor, Q_L, is a function of k. We can get an approximate correction by using the formula

$$Q_0 = Q_L \left(1 + k\right). \tag{8}$$

Subsequently the measured line attenuation (in Np/m) is then calculated

$$\alpha_m = \frac{\pi}{\lambda Q_0}. \tag{9}$$

Note that this attenuation includes both that from the beam coupling impedance as well as that due to the finite resistance of the wire material. We can estimate the attenuation due to the wire material as

$$\alpha_w = \sqrt{\pi \rho_w \epsilon f} \frac{1}{d \ln D/d} \tag{10}$$

where ρ_w is the wire resistivity, ϵ the permitivitty, f the frequency, d the diameter of the inner conductor and D the diameter of the outer conductor (typically the vacuum beam pipe diameter). At very low frequencies the finite skin depth of the inner conductor would also have to be taken into account. Using the corrected attentuation $\alpha = \alpha_m - \alpha_w$, the real longitudinal impedance per unit length can be found to be

$$\Re\{Z\} = 2Z_c\alpha \tag{11}$$

It is more involved too calculate the imaginary impedance using the resonant method. In particular it is necessary to calculate the resonant frequencies of a pipe open at both ends of the same length of the DUT made of a good conducting material (i.e. the physical length is equal to the electrical length). This
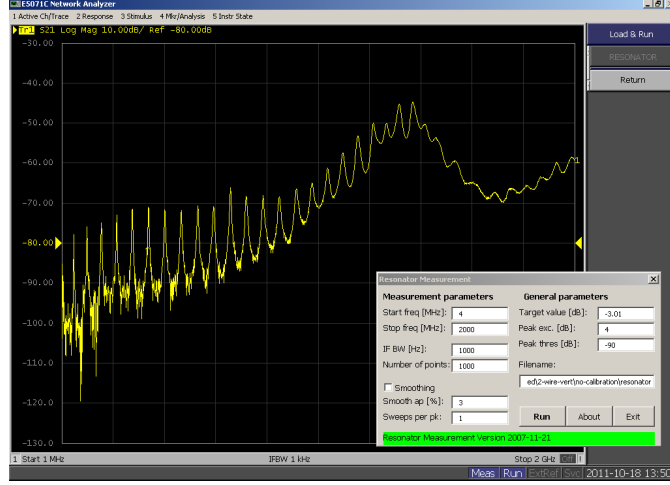
Figure 4: An example of the resonance pattern seen whilst performing measurements using the resonant method. Each peak corresponds to one data point in the final measurements. Taken from measurements of the LHC injection kicker magnets

allows the comparison to the measured resonant frequencies of the DUT, the difference between which is dependent on the imaginary impedance.

If we consider the complex impedance of the two measurements, Z_{DUT} for the DUT and Z_{REF} for a perfectly conducting reference pipe, we can simplify them as

$$Z_{DUT} = R + jX_1 = Z_1 e^{j\phi} \tag{12}$$

$$Z_{REF} = jX_2 = Z_2 e^{j.0} \tag{13}$$

where R is the resistive component of the DUT impedance, $X_{1/2}$ the imaginary component of the impedance (DUT and reference pipe respectively), ϕ is the angle of DUT impedance projected onto a complex plane and $Z_2 = \sqrt{R^2 + X^2}$. If we consider a measured value depedent on the impedance, for example the transmission parameter S_{21} at a resonant peak, we have the following relations

$$S_{21}^{DUT} = S_0 e^{j(\omega_1 t + \phi)} \tag{14}$$

$$S_{21}^{REF} = S_0 e^{k(\omega_2 t)} \tag{15}$$

where S_0 is some normalised scalar, $\omega_{1/2}$ is the frequency of the resonance and $t = \frac{L}{c}$. Thus for a pair of corresponding peaks from resonance measurements for which we have measured ω_1 and ω_2 we can equate $S_{21}^{DUT} = S_{21}^{REF}$ and thus show

$$\phi = t\left(\omega_2 - \omega_1\right). \tag{16}$$

Subsequently we can see that

$$X = Z_{DUT} sin\phi = R\frac{sin\phi}{cos\phi} = Rtan\phi \tag{17}$$

where $R = \Re e(Z)$.

1.3. Transverse Impedance Measurements

The above methods give a general impression of how to carry out coaxial wire measurements of the impedance of accelerator components. Directly applied as described they allow the measurement of the longitudinal impedance of a DUT. However, from a beam stability point of view, it is often more interesting to look at the transverse imedance of a device. In particular it would be useful to have a method of determining the vertical/horizontal dipolar (or driving) impedance and the vertical/horizontal quadrupolar (detuning) impedance of any device. In this section we describe how do this for structures with top/bottom, left/right symmetry and then generalise to asymmetric structures, with illustration from simple examples evaluated using simulations.

To allow a complete explanation of how to verify the methods of measuring transverse impedances, let us first consider the general form of the m-th order ($m = 0, 1, 2, ...$) longitudinal beam coupling impedance, given by [5, 6]

$$\bar{Z}_m = \frac{-1}{I^2} \int dV \bar{\mathbf{E}}_{\mathbf{m}}.\bar{\mathbf{J}}_{\mathbf{m}}^* \tag{18}$$

where $\bar{J}_m$ is the current density of the source. For a beam propogating along the z-axis with an offset a and moment $cos\,(m\theta)$,

$$\bar{\mathbf{J}}_{\mathbf{m}} = \frac{I}{\pi a^{m+1}(1 + \delta_{m0})}\delta\,(r - a)\,cos\,(m\theta)\,exp\,(j\,(\omega t - kz))\,\mathbf{e_z}. \tag{19}$$

The electromagnetic field associated with a given current source $\bar{\mathbf{J}}_{\mathbf{m}}$ is $\left(\bar{\mathbf{E}}_{\mathbf{m}}, \bar{\mathbf{H}}_{\mathbf{m}}\right)$.

It can be seen that any different azimuthal components of the m-th field of order n (i.e. $sin\,(n\theta)$ and $cos\,(n\theta)$ terms) are neglected in this treatment. To allow the treatment of coupling between different azimuthal orders we can define a longitudinal beam coupling impedance $Z_{m,n}$ (where $m, n = 0, \pm1, \pm2, ...$)

$$Z_{m,n} = \frac{-1}{I^2} \int dV \mathbf{E}_{\mathbf{m}}.\mathbf{J}_{\mathbf{n}}^* \tag{20}$$

where

$$\mathbf{J}_{\mathbf{m}} = \frac{I}{\pi a^{|m|+1}}\delta\,(r - a)\,exp\,(jm\theta)\,exp\,(j\,(\omega t - kz))\,\mathbf{e_z}. \tag{21}$$

Importantly, this allows us to see that

$$\bar{\mathbf{J}}_{\mathbf{0}} = \mathbf{J}_{\mathbf{0}}$$

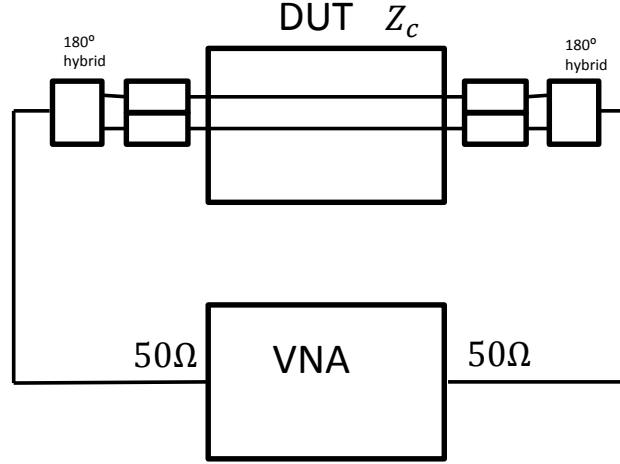$$\bar{\mathbf{J}}_{\mathbf{m}} = \mathbf{J}_{\mathbf{m}} + \mathbf{J}_{-\mathbf{m}}. \tag{22}$$

Figure 5: Measurement setup for measurements of the dipolar beam coupling impedance using the two wire setup for the classical coaxial wire method.

From here we use the principle of superposition for electromagnetic fields (i.e. we neglect any non-linearities of the surrounding materials), and thus can derive

$$\bar{Z}_0 = Z_0 \tag{23}$$

$$\bar{Z}_x = \bar{Z}_1 = Z_{1,1} + Z_{1,-1} + Z_{-1,1} + Z_{-1,-1} = kZ_x^{dip} \tag{24}$$

$$\bar{Z}_x = \bar{Z}_1(\text{cos replaced with sin}) = Z_{1,1} - Z_{1,-1} - Z_{-1,1} + Z_{-1,-1} = kZ_y^{dip} \tag{25}$$

$$\bar{Z}_m = Z_{m,m} + Z_{m,-m} + Z_{-m,m} + Z_{-m,-m}, m = 1, 2, ... \tag{26}$$

From this start we will apply this two both two wire measurements and to displaced single wire measurements.

1.3.1. Two Wire Measurements

It is possible to directly measure the dipolar impedance of a device through the use of a two wire coaxial method. The measurement setup is identical to that of the single wire method, except that two wires, seperated by distance Δ, are placed in the device, and a 180° hybrid is place between the wires and the VNA at both ends of the device. This setup is illustrated in Fig. 1.3.1

The measurements are done in the same way as described in the previous sections for either the classical transmission method or the resonator method. When using the classical coaxial wire method, both wires are individually matched to Z_c. By using two wires each carrying a signal 180° out of phase with one another we produce a field pattern similar to a dipole and thus measure the dipole impedance in either the horizontal or vertical plane depending on the orientation of the two wires.

What is directly measured is the longitudinal impedance of just the dipole impedance, as is to be expected from the Panofsky-Wenzel theorem (see Chap. **??** for further explanation).

For two wire placed as positions $x = \pm a$, the current density is given by [6]

$$
\begin{aligned}
J &= I \left(\delta \left(x - a \right) - \delta \left(x + a \right) \right) \delta(y) exp \left(j \left(\omega t - kz \right) \right) \\
&= \frac{I}{\pi a} \sum_{m=-\infty}^{\infty} exp \left(j \left(2m + 1 \right) \theta \right) exp \left(j \left(\omega t - kz \right) \right) \\
&= 2 \sum_{m=-\infty}^{\infty} a^{|2m+1|} J_{2m+1}.
\end{aligned}
\tag{27}
$$

The impedance is then

$$
\begin{aligned}
Z &= -\frac{1}{I^2} \int dV \left(2 \sum_{m=-\infty}^{\infty} a^{|2m+1|} E_{2m+1} \right) \left(2 \sum_{n=-\infty}^{\infty} a^{|2n+1|} J^{*}_{2n+1} \right) \\
&= 4 \sum_{m,n} a^{|2m+1|+|2n+1|} Z_{2m+1,2n+1} \\
&= (2a)^2 \left(Z_{1,1} + Z_{-1,1} + Z_{1,-1} + Z_{-1,-1} \right) + O(a^4) \\
&= (2a)^2 \bar{Z}_x + O(a^4).
\end{aligned}
\tag{28}
$$

Again using the Panofsky-Wenzel theorem we can deduce that the transverse dipolar impedance $Z_{x/y}^{dip}$ is given by

$$
Z_{x/y}^{dip} = \frac{\bar{Z}_{x/y}}{k} = \frac{c}{\omega} \frac{Z}{\Delta^2}
\tag{29}
$$

where $\Delta = 2a$ and Z is the measured complex impedance.

1.3.2. Structures with Top/Bottom, Left/Right Symmetry

If we consider a source particle at at $x_1 = a_1 cos\theta_1, y_1 = a_1 sin\theta_1$ and a test particle at $x_2 = a_2 cos\theta_2, y_2 = a_2 sin\theta_2$, the source current density is

$$
\begin{aligned}
J_z &= I\delta \left(x - x_1 \right) \delta \left(y - y_1 \right) exp \left(k \left(\omega t - kz \right) \right) \\
&= \sum_{m=-\infty}^{\infty} a_1^{|m|} exp \left(-jm\theta_1 \right) J_m
\end{aligned}
\tag{30}
$$

The impedance would therefore be

$$Z = \frac{-1}{I^2} \int dV \left(\sum_{m=-\infty}^{\infty} a_1^{|m|} exp\left(jm\theta_1\right) E_m \right) \left(\sum_{n=-\infty}^{\infty} a_1^{|n|} exp\left(jn\theta_2\right) J_n^* \right)$$

$$= \sum_{m,n=-\infty}^{\infty} a_1^{|m|} a_2^{|n|} exp\left(-jm\theta_1\right) exp\left(-jn\theta_2\right) Z_{m,n}$$

$$= Z_{0,0} + (x_1 - jy_1) Z_{1,0} + (x_1 + jy_1) Z_{-1,0} + (x_2 + jy_2) Z_{0,1} + (x_2 - jy_2) Z_{0,-1}$$

$$+ (x_1 - jy_1)^2 Z_{2,0} + (x_1 - jy_1)(x_2 - jy_2) Z_{1,-1} + (x_2 - jy_2) Z_{0,-2}$$

$$+ (x_1 - jy_1)(x_2 + jy_2) Z_{1,1} + (x_1 + jy_1)(x_2 - jy_2) Z_{-1,-1}$$

$$+ (x_1 + jy_1)^2 Z_{-2,0} + (x_1 + jy_1)(x_2 - jy_2) Z_{-1,1} + (x_2 - jy_2)^2 Z_{0,2}$$

$$+ O\left((x_1, y_1, x_2, y_2)^3 \right). \tag{31}$$

By applying Panofsky-Wenzel we see

$$kZ_x = \frac{\partial Z}{\partial x_2} = Z_{0,1} + Z_{0,-1} + (x_1 - jy_1) Z_{1,-1} + 2(x_2 - jy_2) Z_{0,-2}$$

$$+ (x_1 - jy_1) Z_{1,1} + (x_1 + jy_1) Z_{-1,-1} + (x_1 + jy_1) Z_{-1,1} + 2(x_2 + jy_2) Z_{0,2}$$

$$+ O\left((x_1, y_1, x_2, y_2)^2 \right)$$

$$= Z_{0,1} + Z_{0,-1} + x_1 \bar{Z}_x + jy_1 \left(-Z_{1,-1} - Z_{1,1} + Z_{-1,-1} + Z_{-1,1} \right)$$

$$+ x_2 \left(2Z_{0,-2} + 2Z_{0,2} \right) + jy_2 \left(-2Z_{0,-2} + 2Z_{0,2} \right) + O\left((x_1, y_1, x_2, y_2)^2 \right) \tag{32}$$

$$kZ_y = \frac{\partial Z}{\partial y_2} = jZ_{0,1} - jZ_{0,-1} - j(x_1 - jy_1) Z_{1,-1} - 2j(x_2 - jy_2) Z_{0,-2}$$

$$+ j(x_1 - jy_1) Z_{1,1} - j(x_1 + jy_1) Z_{-1,-1} + j(x_1 + jy_1) Z_{-1,1} + 2j(x_2 + jy_2) Z_{0,2}$$

$$+ O\left((x_1, y_1, x_2, y_2)^2 \right)$$

$$= j(Z_{0,1} - Z_{0,-1}) + y_1 \bar{Z}_y + jx_1 \left(-Z_{1,-1} + Z_{1,1} + Z_{-1,-1} + Z_{-1,1} \right)$$

$$+ y_2 \left(-2Z_{0,-2} - 2Z_{0,2} \right) + jx_2 \left(-2Z_{0,-2} + 2Z_{0,2} \right) + O\left((x_1, y_1, x_2, y_2)^2 \right). \tag{33}$$

Two properties to note for later use are that

$$\mathbf{J}_{-m}(\omega) = \mathbf{J}_m^*(-\omega) \tag{34}$$

$$Z_{-m,-n}(\omega) = Z_{m,n}^*(-\omega). \tag{35}$$

If we now assume a single wire rather than a source and test particle, such that $x_1 = x_2 = x_0, y_1 = y_2 = y_0$. This gives a source current density

$$J = I\delta\left(x - x_0\right)\delta\left(y - y_0\right)exp\left(j\left(\omega t - kz\right)\right)$$

$$= \frac{I}{2\pi a}\delta\left(r - a\right)\sum_{m=-\infty}^{\infty}exp\left(jm\left(\theta - \theta_0\right)\right)exp\left(jm\left(\theta - \theta_0\right)\right)exp\left(j\left(\omega t - kz\right)\right)$$

$$= \sum_{m=-\infty}^{\infty}a^{|m|}exp\left(-jm\theta_0\right)J_m. \tag{36}$$

We can then define $x_0 = acos\theta_0, y_0 = asin\theta_0$. Entering this into Eqn. 31 gives

$$
\begin{aligned}
Z = \quad & Z_{0,0} + (x_0 - jy_0)Z_{1,0} + (x_0 + jy_0)Z_{-1,0} + (x_0 + jy_0)Z_{0,1} \\
& + (x_0 - jy_0)Z_{0,-1} + (x_0 - jy_0)^2 Z_{2,0} + (x_0 - jy_0)^2 Z_{1,-1} + (x_0 - jy_0)^2 Z_{0,-2} \\
& + (x_0 - jy_0)(x_0 + jy_0)Z_{1,1} + (x_0 + jy_0)(x_0 - jy_0)Z_{-1,-1} + (x_0 + jy_0)^2 Z_{-2,0} \\
& + (x_0 + jy_0)^2 Z_{-1,1} + (x_0 + jy_0)^2 Z_{0,2} + O\left(\left(x_0, y_0\right)^2\right) \\
= \quad & Z_{0,0} + x_0\left(Z_{1,0} + Z_{-1,0} + Z_{0,1} + Z_{0,-1}\right) + jy_0\left(-Z_{-1,0} + Z_{-1,0} + Z_{0,1} - Z_{0,-1}\right) \\
& + x_0^2\left(Z_{1,-1} + Z_{1,1} + Z_{-1,-1} + Z_{-1,1} + Z_{2,0} + Z_{0,-2} + Z_{0,2} + Z_{-2,0}\right) \\
& + y_0^2\left(-Z_{1,-1} + Z_{1,1} + Z_{-1,-1} - Z_{-1,1} - Z_{2,0} - Z_{0,-2} - Z_{0,2} - Z_{-2,0}\right) \\
& + 2jx_0 y_0\left(-Z_{2,0} - Z_{0,-2} + Z_{-2,0} + Z_{0,2} + Z_{-1,1} - Z_{1,-1}\right) \\
= \quad & Z_{0,0} + x_0\left(Z_{1,0} + Z_{-1,0} + Z_{0,1} + Z_{0,-1}\right) + jy_0\left(-Z_{-1,0} + Z_{-1,0} + Z_{0,1} - Z_{0,-1}\right) \\
& + x_0^2\left(\bar{Z}_x + Z_{2,0} + Z_{0,-2} + Z_{0,2} + Z_{-2,0}\right) \\
& + y_0^2\left(\bar{Z}_y - Z_{2,0} - Z_{0,-2} - Z_{0,2} - Z_{-2,0}\right) \\
& + 2jx_0 y_0\left(-Z_{2,0} - Z_{0,-2} + Z_{-2,0} + Z_{0,2} + Z_{-1,1} - Z_{1,-1}\right). \tag{37}
\end{aligned}
$$

It can then be seen that if measurements are made with $x_0 = 0$ and taking different values of y_0 that one obtains data with a parabolic fit in the y_0 axis. By fitting a curve to this we obtain constant (equal to the longitudinal impedance), linear and quadratic terms. Doing the same for $y_0 = 0$ allows us to derive two quadratic terms

$$Z_x^\perp = \left(\bar{Z}_x + kZ_{quad}\right)\frac{1}{k} = Z_x^{dip} + kZ_{quad} \tag{38}$$

$$Z_y^\perp = \left(\bar{Z}_y - kZ_{quad}\right)\frac{1}{k} = Z_y^{dip} - kZ_{quad} \tag{39}$$

$$\tag{40}$$

where $Z_{quad} = \frac{1}{k}\left(Z_{0,2} + Z_{2,0} + Z_{0,-2} + Z_{-2,0}\right) = \frac{2}{k}\left(Z_{0,2} + Z_{0,-2}\right)$, representing the impedance due to the displacement of the test particle in an accelerator. As we can measure $\bar{Z}_{x/y}$ independently using the two wire method we can thus indepedently measure Z_{quad} using a displaced single wire scan in both the x- and y-planes.

It can also be seen that

$$Z_x^\perp + Z_y^\perp = \frac{1}{k}\left(\bar{Z}_x + \bar{Z}_y\right) = Z_x^{dip} + Z_y^{dip} \tag{41}$$

where $\bar{Z}_{x/y}$ can be measured independently which gives a method of obtaining confidence in the wire measurements.

1.3.3. Asymmetric Structures

If Eqn. 37 is transformed from (x, y) coordinates to (a, θ), the result is

$$\begin{aligned}
Z = {}& Z_{0,0} + a\left[cos\theta\left(Z_{-1,0} + Z_{0,1}\right) + jsin\theta\left(Z_{-1,0} + Z_{0,1}\right)cos\theta\left(Z_{1,0} + Z_{0,-1}\right) - jsin\theta\left(Z_{1,0} + Z_{0,-1}\right)\right] \\
& + a^2\left[cos^2\left(Z_{1,1} + Z_{-1,-1}\right) + sin^2\left(Z_{1,1} + Z_{-1,-1}\right)\right] \\
& + a^2\left[cos^2\left(Z_{2,0} + Z_{0,-2} + Z_{1,-1}\right) + 2jsin\theta cos\theta\left(Z_{2,0} + Z_{0,-2} + Z_{1,-1}\right)\right] \\
& - a^2\left[sin^2\left(Z_{2,0} + Z_{0,-2} + Z_{1,-1}\right)\right] \\
& + a^2\left[cos^2\left(Z_{-2,0} + Z_{0,2} + Z_{-1,1}\right) + 2jsin\theta cos\theta\left(Z_{-2,0} + Z_{0,2} + Z_{-1,1}\right)\right] \\
& + a^2\left[sin^2\left(Z_{-2,0} + Z_{0,2} + Z_{-1,1}\right)\right].
\end{aligned} \tag{42}$$

Grouping like terms this becomes

$$\begin{aligned}
Z = {}& Z_{0,0} + a\left[e^{-j\theta}\left(Z_{-1,0} + Z_{0,1}\right) + e^{j\theta}\left(Z_{1,0} + Z_{-0,1}\right)\right] \\
& + a^2\left[\left(Z_{1,1} + Z_{-1,-1}\right) + e^{-2j\theta}\left(Z_{2,0} + Z_{0,-2} + Z_{1,-1}\right) + e^{2j\theta}\left(Z_{-2,0} + Z_{0,2} + Z_{-1,1}\right)\right] \\
= {}& A_1 + ae^{-j\theta}A_2 + ae^{-j\theta}A_3 + a^2e^{-2j\theta}A_4 + a^2e^{2j\theta}A_5 + a^2A_6
\end{aligned} \tag{43}$$

where $A_1 = Z_{0,0}$, $A_2 = Z_{0,1} + Z_{-1,0}$, $A_3 = Z_{0,-1} + Z_{1,0}$, $A_4 = Z_{0,2} + Z_{-1,1} + Z_{-2,0}$, $A_5 = Z_{2,0} + Z_{1,-1} + Z_{0,-2}$ and $A_6 = Z_{1,1} + Z_{-1,-1}$. Taking the earlier definition of Z_{quad} it can be deduced that

$$Z_{quad} = \left(A_4 + A_5 + A_6 - \bar{Z}_x\right)\frac{1}{k} = \frac{A_4 + A_5 + A_6}{k} - Z_x^{dip} \tag{44}$$

$$= \left(A_4 + A_5 - \frac{\bar{Z}_x - \bar{Z}_y}{2}\right)\frac{1}{k} = \frac{A_4 + A_5}{k} - \frac{Z_x^{dip} - Z_y^{dip}}{2}. \tag{45}$$

Consideration of Eqn. 43 lets it be seen that

$$A_4 + A_5 + A_6 = \frac{Z\left(a, 0\right) + Z\left(a, \pi\right) - 2Z\left(0, 0\right)}{2a^2} \tag{46}$$

$$A_4 + A_5 = \frac{Z\left(a, 0\right) + Z\left(a, \pi\right) - Z\left(a, \frac{\pi}{2}\right) - Z\left(a, \frac{3\pi}{2}\right)}{2a^2}. \tag{47}$$

The constant impedance can also be seen to be found by taking a linear fit of the longitudinal impedance of a wire displaced in either the $\theta = 0$ or $\theta = \pi/2$ plane, and taking the linear term of the fit.

12

1.4. Measurements on Example Geometries

In this section shall be presented a number of example analyses of coaxial wire measurements done on geometries exhibiting top/bottom, left/right symmetry and an asymmetric structure. This permits a step-by-step guide to analysis of the wire measurements, which may not be immediately clear from the mathematical introduction. These simulations are carried out using both Ansoft HFSS and Maxwell using a driven modal solution.

The simulations with HFSS are carried out in the following manner: the measurement system is simulated by placing waveguide ports at either end of the geometry with a conducting cylinder placed as the inner conductor of the coaxial system. The transmission parameters are then acquired as a result of the simulations. The wire may then be displaced as neccessary for the displaced single wire measurements. For two wire measurements a quarter geometry may be simulated, using suitable boundary conditions on the quarter geometry.

Maxwell is a frequency domain code optimised for low frequencies (less thans 10s of MHz). It does not permit the use of waveguide ports, however it does allow the definition of current segments with phase changes between them. By considering the current (either a single current segment to simulate a single wire, or two current carrying segments $180°$ out of phase for two wires) to be the equivalent of a beam current, and assuming the inclusion of the current carrying component is a negligible perturbation to the geometry, the impedance can be found by summing the power loss in the system. This can be seen to be equivalent to the beam induced heating experienced by a beam interacting with an impedance.

This can be thought of by comparing the system to a homogenous transmission line [7]. The power P of a wave travelling along the line is given by

$$P = P_0 e^{-2\alpha z} \tag{48}$$

where P_0 is the power at the beginning of the transmission line, α is the attenuation coefficient and z the distance along the line. By differentiation it can be seen that

$$\alpha = -\frac{1}{2P}\frac{dP}{dz} \approx \frac{1}{2P}\frac{\delta P}{\delta z} \tag{49}$$

where δP is the power lost over the short distance δz. The transmission parameter of a line S_{21} is given by

$$S_{21} = e^{-\alpha \delta z}. \tag{50}$$

If the impedance is evaluated using the log formula ($Z = Z_c ln S_{21}$), it can be seen that the real impedance is subsequently given by

$$\Re e\left(Z\right) = Z_c \frac{2\delta P}{P}. \tag{51}$$

Assuming a peak current I_0 on the wire, $P = I_0^2 Z_c/2$, which gives
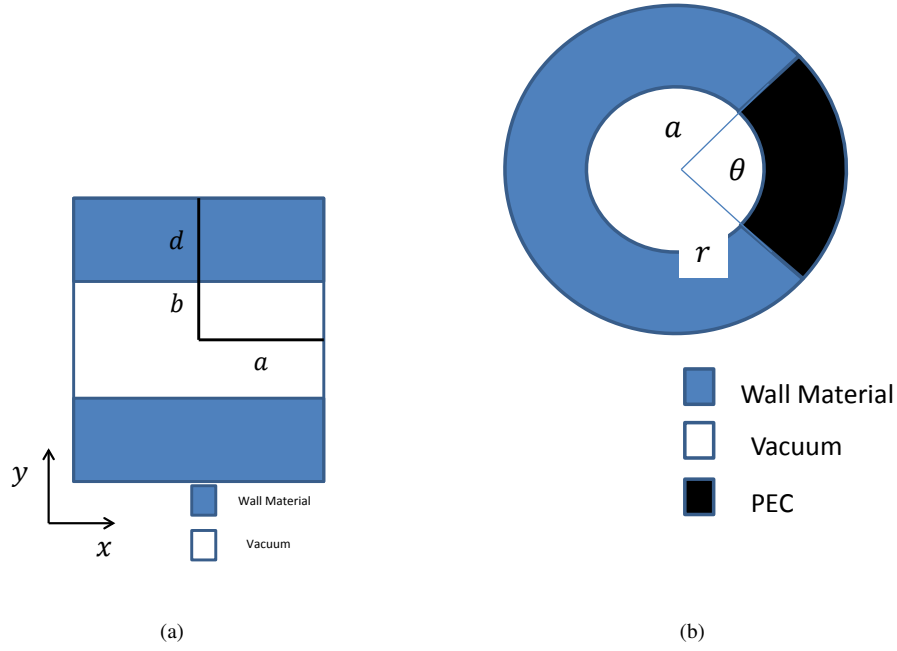
Figure 6: The geometries used for coaxial wire measurement simulations. For the geometry with top/bottom, left/right symmetry we use the Tsutsui model (6(a)) using two parallel plates. For the asymmetric structure we use the Zannini-model for a c-core ferrite kicker magnet (6(b)), which generates a constant term and a noticeable asymmetric term.

$$\Re e\left(Z\right) = \frac{2\delta P}{I_0^2}. \tag{52}$$

To acquire the transverse impedance for two wire simulations it is simply neccesary to normalise by the wavenumber $k = \omega/c$ and the seperation of the wire Δ

$$Z_{dip} = \frac{c}{\omega\Delta^2}\frac{2\delta P}{I_0^2}. \tag{53}$$

1.4.1. Structure with Top/Bottom, Left/Rght Symmetry

For the structure exhibiting top/bottom, left/right symmetry we use the Tsutsui model of two parallel plates as shown in Fig. 6(a). We use this due to the model allowing the prediction of the longitudinal, dipolar and quadrupolar impedances for a wide variety of materials and frequency ranges [8–10]. For these simulations a short segment of a Tsutsui geometry is simulated using two different materials, in this case graphite, to represent a structure with a poor conductivity ($\sigma_{graphite} = 7 \times 10^4 Sm^{-1}$), and 4A4 ferrite, to represent a magnetically lossy material (in this case, $\epsilon_r = 10$, $\sigma_{4A4} = 10^{-6} Sm^{-1}$ (a mild conductivity is applied to prevent static build up in ferrite components in accelerators)), and $\mu_r = \mu^{'} + j\mu^{"}$, shown in Fig. 7.). In both cases the following dimensions are used: $a = 25mm$, $b = 5mm$, $d = 5mm$. A structure 150mm in length is used to reduce numerical noise due to the small losses given by the short length of the simulated DUT.
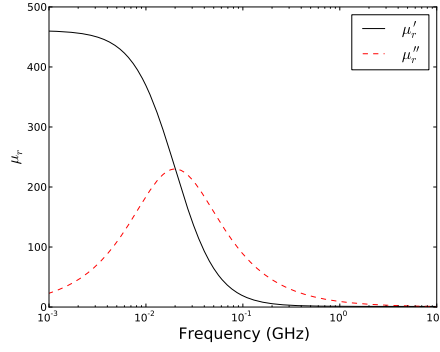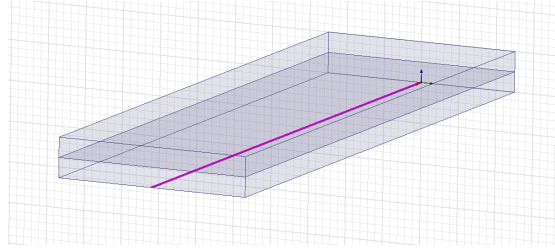
Figure 7: The complex permeability of 4A4 ferrite.

Figure 8: An example of the simulation model used for coaxial wire simulations. In this case a displaced single wire between two ferrite plates. The wire is highlighted in purple.

1.4.2. Two Parallel Ferrite Plates

For the simulations of two parallel ferrite plates the following parameters were used; for the displaced single wire measurements a wire of 0.3mm in radius, and the following displacement used to acquire the total transverse terms:

1. In the horizontal axis - displaced between -6mm to +6mm at intervals of 2mm
2. In the vertical axis - displaced between -4mm to +4mm at intervals of 2mm.

For the two wire simulations, two wires of radius 0.3mm are used, with a seperation of 4mm in the x-dimension, and 3mm in the y-dimension. 4 simulation configurations are used described below:

1. an adaptive mesh generation set to a convergence criteria of S_{21} diverging by less than 0.005 between two subsequent solutions, at an adaptive frequency of 20MHz solving to a second order basis. A discrete frequency sweep is then carried out in the range 1-10MHz at 1MHz intervals.
2. an adaptive mesh generation set to a convergence criteria of S_{21} diverging by less than 0.005 between two subsequent solutions, at an adaptive frequency of 200MHz solving to a second order basis. A discrete frequency sweep is then carried out in the range 10-100MHz at 10MHz intervals.
3. an adaptive mesh generation set to a convergence criteria of S_{21} diverging by less than 0.005 between two subsequent solutions, at an adaptive frequency of 2GHz solving to a second order basis. A discrete frequency sweep is then carried out in the range 100MHz-1GHz at 100MHz intervals.
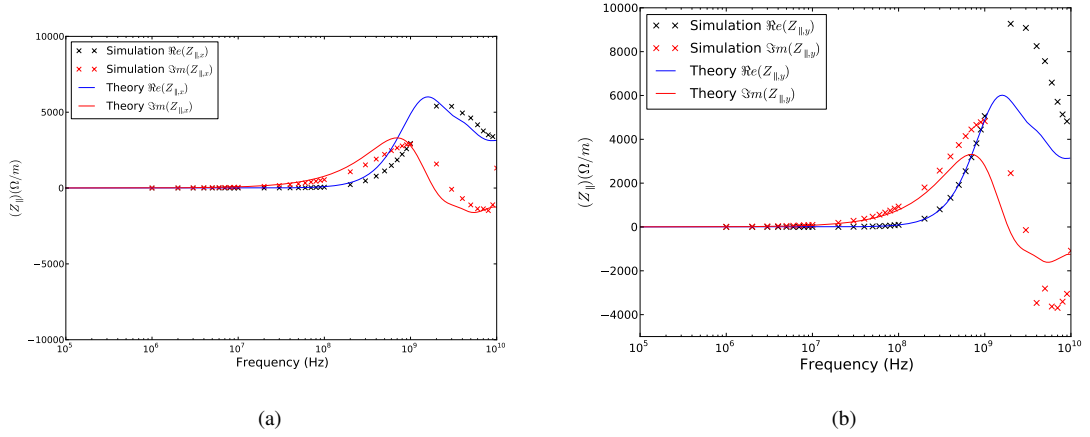
(a)   (b)

Figure 9: The longitudinal impedance of two parallel ferrite plates simulated using a longitudinal coaxial wire. Presented are is the impedance as measured in the horizontal plane (9(a)) and in the vertical plane 9(b).
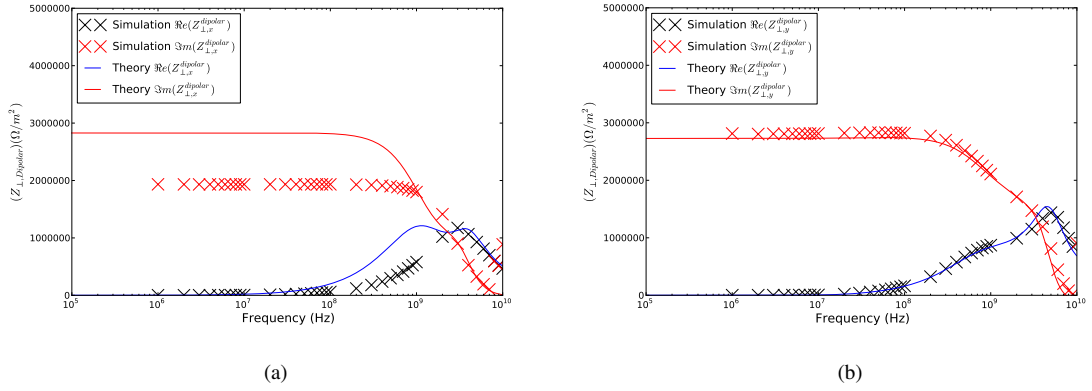

(a)   (b)

Figure 10: The dipolar impedance of two parallel ferrite plates simulated using two longitudinal coaxial wires. Presented are is the impedance as measured in the horizontal plane (10(a)) and in the vertical plane 10(b).

4. an adaptive mesh generation set to a convergence criteria of S_{21} diverging by less than 0.005 between two subsequent solutions, at an adaptive frequency of 10GHz solving to a second order basis. A discrete frequency sweep is then carried out in the range 1-10GHz at 1GHz intervals.

These parameters are used to benefit from an appropriate mesh count for the given frequency range, thus increasing simulation speed by not using a high density mesh at frequencies where no benefits would be gained.

The longitudinal impedance is as determined by taking the constant term for a series of simulated displaced wire measurements in both the vertical and horizontal planes is shown in Fig. 9. It can be seen that in the frequency range below 100MHz the agreement between the coaxial wire results and the analytical results is very good in both the vertical and horizontal plane. Above 100MHz the agreement for the real components is very good for both results, however the imaginary component in the vertical plane displays some substantial disagreement. This is likely due to the high mesh density required to correctly
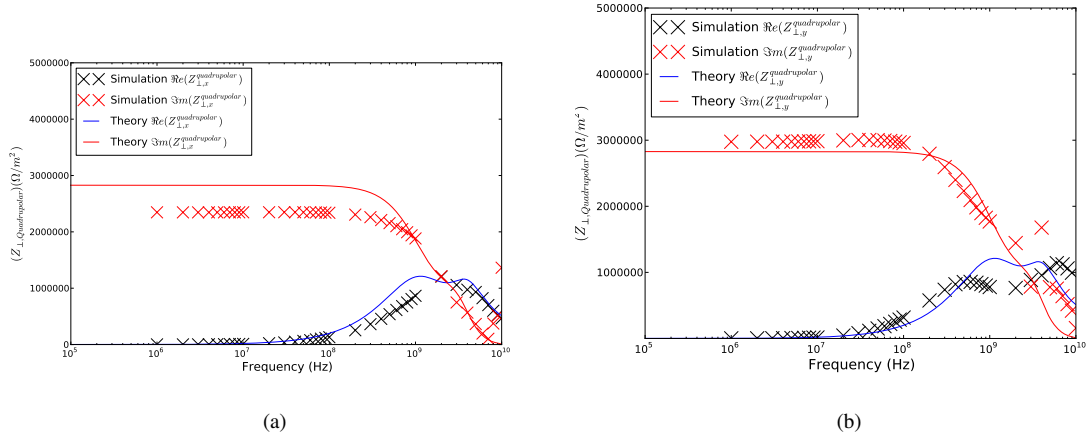
16

(a)

(b)

Figure 11: The quadrupolar impedance of two parallel ferrite plates simulated using a combination of displaced single wire simulated measurements and two wire simulated mesurements. Presented are is the impedance as measured in the horizontal plane (11(a)) and in the vertical plane 11(b).

evaluate the phase change along the length of the simulated structure. A higher mesh density may correct this, however limits of computational resource presently make this unfeasible.

The agreement between the simulations of the vertical dipolar impedance and the theoretical model is excellent across all frequencies for both the real and imaginary components. The agreement below 100MHz and above 1GHz is very good for the horizontal dipolar, with some divergence in the constant term of the imaginary impedance. The key difference is the failure of the coaxial method to resolve one of the peaks in the real impedance. The results for the dipolar impedance are shown in Fig. 10.

The results for the quadrupolar impedance are shown in Fig. 11. The vertical simulations agree well with the theory, correctly identifying the two peaks in the quadrupolar impedance. The agreement for the horizontal simulations with theory is less good. This can be explained by the derivation of the horizontal quadrupolar being highly dependent on the quality of the horizontal dipolar impedance results due to them cancelling each other to form the total transverse impedance. As the horizontal dipolar impedance does not resolve the the subpeaks neither does the horizontal quadrupolar impedance calculations.

1.4.3. Two Parallel Graphite Plates

For the simulations of measurements of two parallel graphite plates, two different methods were used. Due to the non-ferritic properties of the graphite, it is possible to use Maxwell3D to simulate the power loss at lower frequencies, thus acquiring the real component of the impedance for low frequencies, in addition to using the classical coaxial wire method at higher frequencies in HFSS.

For the simulations of the power loss in Maxwell3D the following parameters were used; for the displaced single wire measurements a wire of 0.5mm in radius is modelled, and the following displacement used to acquire the total transverse terms:

1. In the horizontal axis - displaced between -6mm to +6mm at intervals of 2mm

17

2. In the vertical axis - displaced between -4mm to +4mm at intervals of 2mm.

For the two wire simulations, two wires of radius 0.3mm are modelled, with a seperation of 8mm in the x-dimension, and 4mm in the y-dimension. Five simulation configurations are used as described below:

1. an adaptive mesh generation set to a convergence criteria of S_{21} diverging by less than 0.005 between two subsequent solutions, at an adaptive frequency of 20kHz solving to a second order basis. A discrete frequency sweep is then carried out in the range 1-10kHz at 1kHz intervals.

2. an adaptive mesh generation set to a convergence criteria of S_{21} diverging by less than 0.005 between two subsequent solutions, at an adaptive frequency of 200kHz solving to a second order basis. A discrete frequency sweep is then carried out in the range 10-100kHz at 10kHz intervals.

3. an adaptive mesh generation set to a convergence criteria of S_{21} diverging by less than 0.005 between two subsequent solutions, at an adaptive frequency of 2MHz solving to a second order basis. A discrete frequency sweep is then carried out in the range 100kHz-1MHz at 100kHz intervals.

4. an adaptive mesh generation set to a convergence criteria of S_{21} diverging by less than 0.005 between two subsequent solutions, at an adaptive frequency of 10MHz solving to a second order basis. A discrete frequency sweep is then carried out in the range 1-10MHz at 1MHz intervals.

5. an adaptive mesh generation set to a convergence criteria of S_{21} diverging by less than 0.005 between two subsequent solutions, at an adaptive frequency of 100MHz solving to a second order basis. A discrete frequency sweep is then carried out in the range 10-100MHz at 10MHz intervals.

These parameters are used to benefit from an appropriate mesh count for the given frequency range, thus increasing simulation speed by not using a high density mesh at frequencies where no benefits would be gained.

For the simulations of the single displaced wire in HFSS the following parameters were used; for the displaced single wire measurements a wire of 0.3mm in radius is modelled, and the following displacements to acquire the total transverse terms:

1. In the horizontal axis - displaced between -6mm to +6mm at intervals of 2mm

2. In the vertical axis - displaced between -4mm to +4mm at intervals of 2mm.

For the two wire simulations, two wires of radius 0.3mm are modelled, with a seperation of 4mm in the x-dimension, and 3mm in the y-dimension. Three simulations configuration are used as described below:

1. an adaptive mesh generation set to a convergence criteria of S_{21} diverging by less than 0.005 between two subsequent solutions, at an adaptive frequency of 20MHz solving to a second order basis. A discrete frequency sweep is then carried out in the range 1-10MHz at 1MHz intervals.

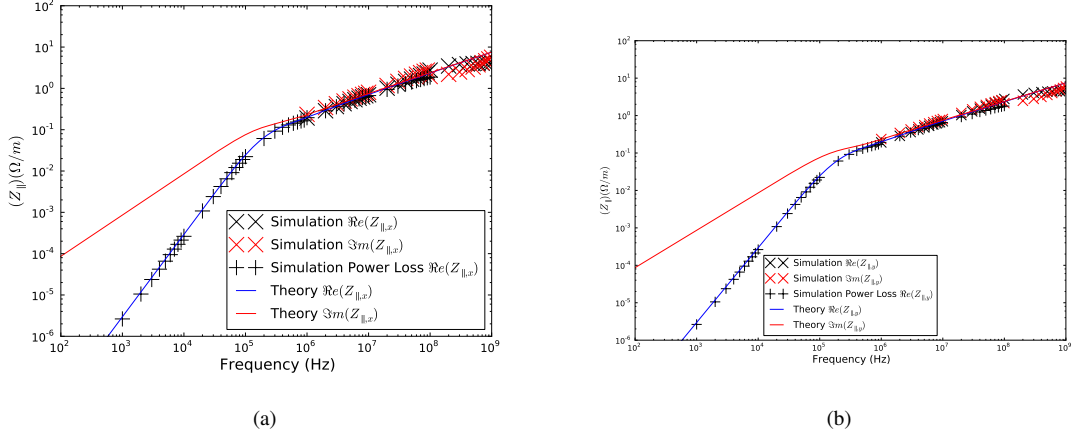(a)   (b)

Figure 12: The longitudinal impedance of two parallel graphite plates as measured by taking the constant term of a quadratic equation fitted to a series of displaced single wire measurements. Shown are measurements acquired from fitting displacements in 12(a) horizontal axis and in 12(b) the vertical axis.
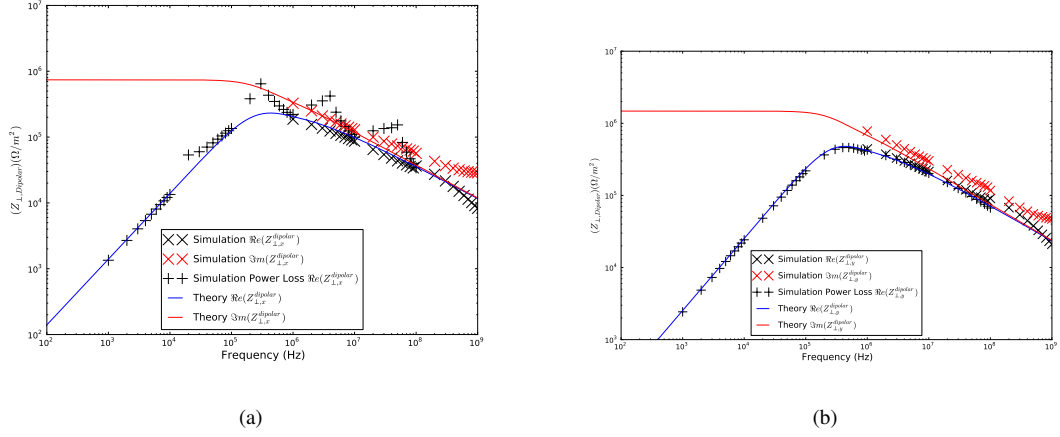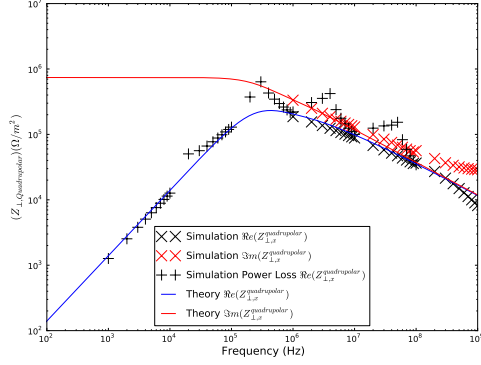

(a)   (b)

Figure 13: The dipolar impedance of two parallel graphite plates measured using two longitudinal coaxial wires. Presented is the impedance as measured in the horizontal plane (13(a)) and in the vertical plane 13(b).

2. an adaptive mesh generation set to a convergence criteria of S_{21} diverging by less than 0.005 between two subsequent solutions, at an adaptive frequency of 200MHz solving to a second order basis. A discrete frequency sweep is then carried out in the range 10-100MHz at 10MHz intervals.

3. an adaptive mesh generation set to a convergence criteria of S_{21} diverging by less than 0.005 between two subsequent solutions, at an adaptive frequency of 2GHz solving to a second order basis. A discrete frequency sweep is then carried out in the range 100MHz-1GHz at 100MHz intervals.

As before these parameters are used to benefit from an appropriate mesh count for the given frequency range, thus increasing simulation speed by not using a high density mesh at frequencies where no benefits would be gained.

The longitudinal impedance can be seen in Fig. 12. It can be seen that the agreement for both the real component is excellent across the entire frequency range, for simulations using both the classical coaxial

Figure 14: The quadrupolar impedance of two parallel graphite plates measured using a combination of displaced single wire measurements and two wire mesurements. Presented is the impedance as measured in the horizontal plane (14(a)) and in the vertical plane 14(b).

wire method and the power loss method of Maxwell3D. The agreement is also good for the imaginary component over much of the frequency range, becoming worse above 100MHz. This is likely due to insufficient mesh density to catch the relatively small phase shift at this frequency range.

The agreement between simulations and theory for the vertical dipolar impedance can be seen to be very good over the entire frequency range also (see Fig. 13(b)). The results at low frequencies (below 100kHz) for the power loss method and at all frequencies for the classical coaxial wire method for the horizontal dipolar impedance agree very well with theory (see Fig. 13(a)).

1.4.4. C-Core Ferrite Kicker

To test the measurement method for an asymmetric structure a model of the c-core ferrite kicker magnet was used, as shown in Fig.6(b), the analytical details of which are given in [11]. Key in this type of structure is that it predictsa non-zero constant transverse impedance term as well as the quadrupolar terms, thus we may completely evaluate the asymmetric measurement method. For these simulations a structure of $a = 15$mm, $r = 20$mm, $\theta = \pi/2$, and 100mm in length was used. Simulations were carried out using the classical coaxial wire method as simulated in HFSS.

The following parameters were used for the simulations; wire of 0.2mm in radius, and the following displacement used to acquire the total transverse terms:

1. In the horizontal axis - displaced between -5mm to +5mm at intervals of 1mm

2. In the vertical axis - displaced between -5mm to +5mm at intervals of 1mm.

For the two wire simulations, two wires of radius 0.2mm are modelled, with a seperation of 2mm in the x-dimension, and 2mm in the y-dimension. Four simulation configurations are used described below:

1. an adaptive mesh generation set to a convergence criteria of S_{21} diverging by less than 0.005 between two subsequent solutions, at an adaptive frequency of 20MHz solving to a second order basis. A discrete frequency sweep is then carried out in the range 1-10MHz at 1MHz intervals.

2. an adaptive mesh generation set to a convergence criteria of S_{21} diverging by less than 0.005 between two subsequent solutions, at an adaptive frequency of 200MHz solving to a second order basis. A discrete frequency sweep is then carried out in the range 10-100MHz at 10MHz intervals.

3. an adaptive mesh generation set to a convergence criteria of S_{21} diverging by less than 0.005 between two subsequent solutions, at an adaptive frequency of 2GHz solving to a second order basis. A discrete frequency sweep is then carried out in the range 100MHz-1GHz at 100MHz intervals.

4. an adaptive mesh generation set to a convergence criteria of S_{21} diverging by less than 0.005 between two subsequent solutions, at an adaptive frequency of 10GHz solving to a second order basis. A discrete frequency sweep is then carried out in the range 1-10GHz at 1GHz intervals.

These parameters are used to benefit from an appropriate mesh count for the given frequency range, thus increasing simulation speed by not using a high density mesh at frequencies where no benefits would be gained.

It can be seen that the longitudinal impedance agrees well over the entire frequency range below 1GHz (Fig. 15(a)). The analytical calculations breakdown above 1GHz due to the family of Bessel functions used for the calculations being optimised for low frequency calculations. Similarly the agreement for the dipolar impedance can be seen to be exceptionally good over the majority of the frequency range, with an increasing descrepency at high frequencies (Fig. 15(b)).

To test the asymmetric method we should look at the constant and quadrupolar terms. In this case it can be seen that the agreement with the constant transverse term is exceptionally good across the entire frequency range (Fig. 15(d)). The agreement for the quadrupolar impedance is good in the range of frequencies below 1GHz. Above this the unsuitability of the family of Bessel functions used for this frequency range becomes more apparent and the simulated and analytical results diverge.

It can be seen that the proposed asymmetric method can replicate the beam coupling impedance of an asymmetric structure, correctly predicting both longitudinal and transverse (dipolar, quadrupolar and constant) terms below 1GHz.
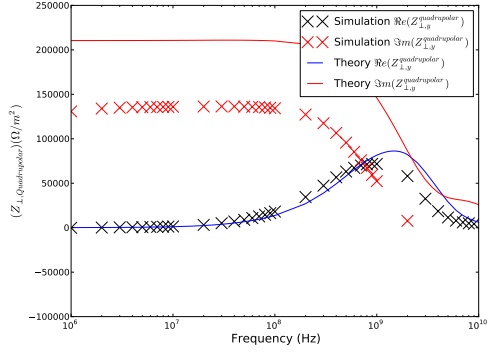
References

[1] R. L. Gluckstern, R. Li, Analysis of coaxial wire measurement of longitudinal coupling impedance, Part. Accel. 29 (DOE-ER-10666-1. CONF-890803-7) (1989) 159–166. 8 p.

[2] V. G. Vaccaro, Coupling impedance measurements: an improved wire method, Tech. Rep. INFN-TC-94-023, INFN, Rome (Nov 1994).
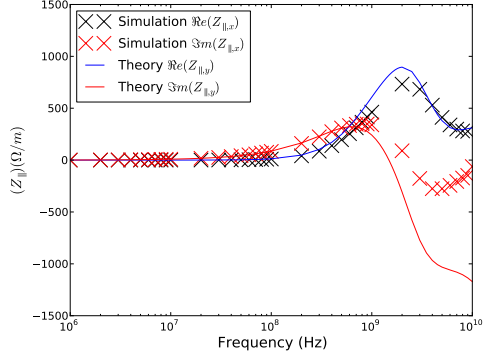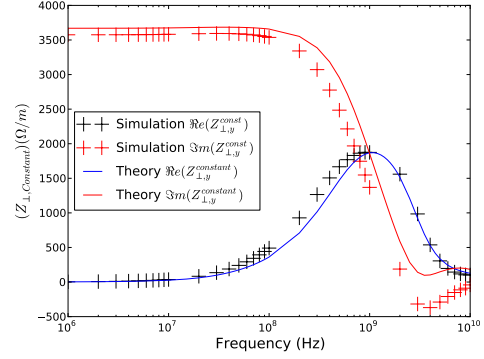
(a)
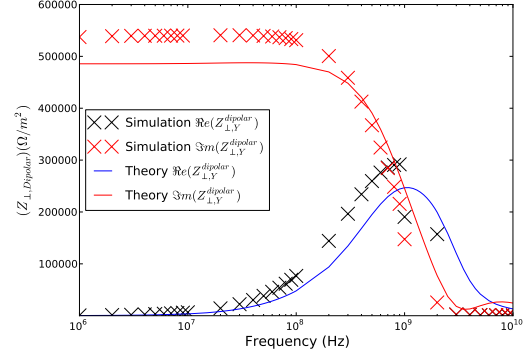
(b)

(c)

(d)

Figure 15: The impedance of the c-core ferrite kicker as acquired by simulating the classical coaxial wire method in HFSS. Shown is the 15(a) longitudinal impedance, 15(b) the dipolar impedance, 15(c) the quadrupolar impedance and 15(d) the constant transverse impedance.

[3] H. Hahn, Interpretation of coupling impedance bench measurements, Phys. Rev. ST Accel. Beams 7 (2004) 012001. `doi:10.1103/PhysRevSTAB.7.012001`.
URL `http://link.aps.org/doi/10.1103/PhysRevSTAB.7.012001`

[4] E. Jensen, An improved log-formula for homogeneously distributed impedance, Tech. Rep. CERN-PS-RF-NOTE-2000-001, CERN, Geneva (Jan 2000).

[5] A. W. Chao, Physics of collective beam instabilities in high energy accelerators, Wiley, New York, NY, 1993.

[6] H. Tsutsui, On single wire technique for transverse coupling impedance measurement, Tech. Rep. SL-Note-2002-034-AP, CERN, Geneva (Oct 2002).

[7] T. Kroyer, Simulation of the low-frequency collimator impedance, Tech. Rep. CERN-AB-Note-2008-017, CERN, Geneva (Apr 2008).

[8] H. Tsutsui, Some simplified models of ferrite kicker magnet for calculation of longitudinal coupling impedance, Tech. Rep. CERN-SL-2000-004-AP, CERN, Geneva (Jan 2000).

[9] H. Tsutsui, L. Vos, Transverse coupling impedance of a simplified ferrite kicker magnet model, Tech. Rep. LHC-PROJECT-NOTE-234, CERN, Geneva (Sep 2000).

[10] B. Salvant, N. Mounet, C. Zannini, E. Métral, G. Rumolo, Quadrupolar transverse impedance of simple models of kickers, Tech. Rep. CERN-ATS-2010-076 (Jun 2010).

[11] C. Zannini, G. Rumolo, V. Vaccaro, Effect of the tem mode on the kicker impedance, Tech. Rep. CERN-ATS-2012-134, CERN, Geneva (May 2012).